

# Thermoelectric Performance of IV–VI Compounds with Octahedral-Like Coordination: A Chemical-Bonding Perspective

Matteo Cagnoni, Daniel Führen, and Matthias Wuttig\*

Thermoelectric materials provide a challenge for materials design, since they require optimization of apparently conflicting properties. The resulting complexity has favored trial-and-error approaches over the development of simple and predictive design rules. In this work, the thermoelectric performance of IV–VI chalcogenides on the tie line between GeSe and GeTe is investigated. From a combination of optical reflectivity and electrical transport measurements, it is experimentally proved that the outstanding performance of IV–VI compounds with octahedral-like coordination is due to the anisotropy of the effective mass tensor of the relevant charge carriers. Such an anisotropy enables the simultaneous realization of high Seebeck coefficients, due to a large density-of-states effective mass, and high electrical conductivity, caused by a small conductivity effective mass. This behavior is associated to a unique bonding mechanism by means of a tight-binding model, which relates band structure and bond energies; tuning the latter enables tailoring of the effective mass tensor. The model thus provides atomistic design rules for thermoelectric chalcogenides.


Conversion of waste heat into electricity through thermoelectric power generators could help reducing the carbon footprint of mankind. Materials, which can be employed in such generators, require a high thermoelectric figure of merit  $zT$ , defined as

$$zT = \frac{S^2 \sigma}{k_L + L\sigma T} T \quad (1)$$

where  $S$ ,  $\sigma$ , and  $k_L$  are the Seebeck coefficient, the electrical conductivity, and the lattice thermal conductivity, respectively,

M. Cagnoni, D. Führen, Prof. M. Wuttig  
I. Institute of Physics (IA)  
RWTH Aachen University  
52056 Aachen, Germany  
E-mail: wuttig@physik.rwth-aachen.de

Prof. M. Wuttig  
JARA-FIT Institute Green-IT  
RWTH Aachen University and Forschungszentrum Jülich  
52056 Aachen, Germany

 The ORCID identification number(s) for the author(s) of this article can be found under <https://doi.org/10.1002/adma.201801787>.

© 2018 RWTH Aachen University. Published by WILEY-VCH Verlag GmbH & Co. KGaA, Weinheim. This is an open access article under the terms of the Creative Commons Attribution-NonCommercial-NoDerivs License, which permits use and distribution in any medium, provided the original work is properly cited, the use is non-commercial and no modifications or adaptations are made.

DOI: 10.1002/adma.201801787

while  $L$  is the Lorentz number and  $T$  is the temperature.<sup>[1,2]</sup> Inspection of the figure of merit reveals just a few of the interdependencies that pose a challenge when designing thermoelectric materials. For example, a large effective mass enhances the Seebeck coefficient but deteriorates the electrical conductivity, while a large carrier concentration improves the electrical conductivity but reduces the Seebeck coefficient. Furthermore, a high electrical conductivity results in a large electronic contribution to the thermal conductivity,  $L\sigma T$ . The task to find novel thermoelectrics hence appears to be rather daunting.

In the past, the following rules have been derived to optimize thermoelectric energy conversion. Maximizing the power factor  $S^2\sigma$  by optimizing the carrier concentration through doping has been the first approach to achieve a large thermoelectric figure of merit. This strategy has

been applied to materials containing softly bonded heavy atoms to ensure a slow phonon group velocity, resulting in a small lattice thermal conductivity.<sup>[3]</sup> Subsequently, researchers have tried to maximize phonon scattering utilizing large unit cells that enhance Umklapp scattering,<sup>[4]</sup> by filling lattices with weakly bound atoms that rattle incoherently<sup>[5]</sup> and by introducing point defects and nanostructures.<sup>[6–8]</sup> Finally, multivalley transport has allowed avoiding the trade-off between Seebeck coefficient  $S$  and electrical conductivity  $\sigma$ , hence achieving superior power factors  $S^2\sigma$ .<sup>[9,10]</sup>

In recent years, binary chalcogenides have returned into the focus of the thermoelectric community. Many compounds with an excellent thermoelectric performance are based on PbTe,<sup>[11–13]</sup> PbSe,<sup>[14]</sup> GeTe,<sup>[15]</sup> and Bi<sub>2</sub>Te<sub>3</sub>.<sup>[16]</sup> Lately, the highest figure of merit ever reported has been found in single crystals of SnSe.<sup>[17]</sup> The outstanding properties have been attributed to the complex band structure<sup>[18,19]</sup> as well as the intrinsically low lattice thermal conductivity, which has been associated to anharmonic effects<sup>[20]</sup> due to either lone pairs<sup>[21,22]</sup> or resonant bonding.<sup>[23,24]</sup>

These findings raise the question of whether the origin of the large power factor could lie in the chemical bonding properties of the corresponding material. As a first attempt to address this point, a map has been created for binary chalcogenides sorting them according to their bonding properties.<sup>[25,26]</sup> The result is shown in **Figure 1**, where a map of compounds with an average of 3 valence p electrons per lattice site ( $N_p = 3$ ), such as GeTe or Sb<sub>2</sub>Te<sub>3</sub>, is depicted. The compounds are arranged according

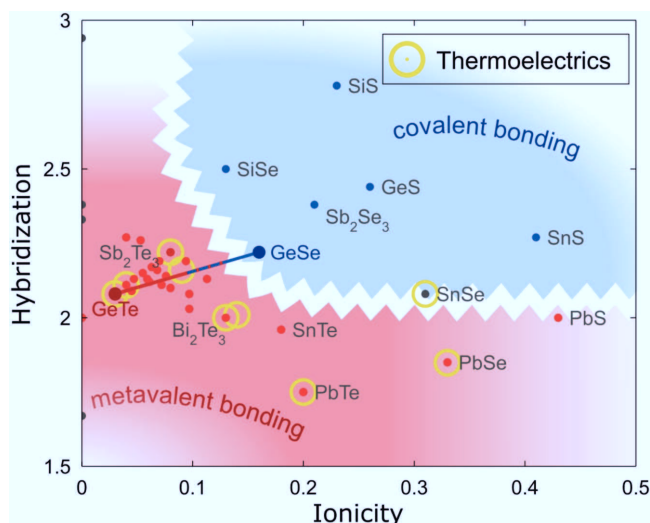


**Figure 1.** Map for various group V elements, and IV–VI as well as  $V_2V_3$  compounds. The materials are sorted according to ionicity and s-p hybridization. Materials that exhibit metavalent bonding are denoted in red, while materials that do not exhibit metavalent bonding are shown in blue. Yellow circles highlight single-phase materials with a recorded maximum  $zT$  above 0.7. Interestingly, most thermoelectric materials are located in the red region of the map. This implies that these materials possess common intrinsic physical properties beneficial for thermoelectric performance.

to increasing ionicity and s-p mixing along the  $x$ - and  $y$ -axis, respectively.<sup>[26]</sup> The blue region marks materials which are characterized by ordinary covalent bonding. On the other hand, materials in the red region exhibit a large optical dielectric constant  $\epsilon_\infty$ , high effective coordination numbers, and large Born effective charges  $Z^*$ . These findings have been attributed to a different bonding mechanism, which has been called resonant bonding in the past.<sup>[27–29]</sup> Lately, the name metavalent bonding has been suggested instead, to distinguish from resonant bonding in the  $\pi$ -orbital systems of benzene and graphene.<sup>[30]</sup> Metavalent materials, also called incipient metals, exhibit a unique bonding mechanism between covalent and metallic bonding. Unlike metals, where electron delocalization is crucial, and unlike covalent compounds, where instead valence electrons are localized, the electrons responsible for chemical bonding show both characteristics of localization and delocalization. The unique nature of this bonding mechanism also becomes evident in laser-assisted field evaporation performed by atom probe tomography experiments, which reveal a bond-breaking mechanism drastically different from metallic and covalent bonding.<sup>[31]</sup> In Figure 1, yellow circles represent single-phase chalcogenides with a recorded maximum  $zT$  larger than 0.7, i.e., with thermoelectric behavior.<sup>[1,12–15,17,32,33]</sup> Interestingly, most yellow circles occur in the red region of the map, where metavalent bonding prevails. This is already a strong hint for a link between chemical bonding and thermoelectric performance.

To verify that it is not just due to coincidence, it is appropriate to study the response of the thermoelectric performance to the controlled breakdown of metavalent bonding. A suitable system for this purpose is  $\text{GeSe}_x\text{Te}_{1-x}$ , which is highlighted in Figure 1. While crystalline GeTe exhibits a good thermoelectric performance,<sup>[34]</sup> the electron transport properties prevent pure

GeSe from reaching a significant figure of merit.<sup>[35]</sup> These two compounds can be alloyed without phase separation. GeTe-rich alloys adopt a rhombohedral phase, which corresponds to a slightly distorted rock-salt structure, while the GeSe-rich alloys favor an orthorhombic phase. The rhombohedral phase is observed below a Se molar fraction of 80%, whereas above 80 at% Se the compounds become orthorhombic.<sup>[25,26,29]</sup> Furthermore, a hexagonal phase is found for Se molar fraction values between 55% and 80% in  $\text{GeSe}_x\text{Te}_{1-x}$ ,<sup>[29,36,37]</sup> where also the rhombohedral phase can exist. Hence, we have a range of stoichiometries, where alloys occur with two different atomic arrangements. Furthermore, there is compelling evidence that these two phases also differ significantly in their bonding characteristics.<sup>[29–31]</sup> While the rhombohedral phase utilizes metavalent bonding, as evidenced by large values of  $\epsilon_\infty$ ,  $Z^*$  and probability for multiple ions detected per laser pulse in laser-assisted field evaporation studies, the hexagonal phase employs ordinary covalent bonding, as substantiated by significantly smaller values of such quantities. It hence suggests itself to study the thermoelectric performance of these different phases.

Seebeck coefficient  $S$ , electrical conductivity  $\sigma$ , power factor  $S^2\sigma$ , and carrier concentration  $n$  have been experimentally determined for several  $\text{GeTe}_x\text{Se}_{1-x}$  alloys with different composition and structure. Room-temperature results as a function of stoichiometry and crystalline phase are reported in Figure 2; data for orthorhombic GeSe has been taken from literature.<sup>[35]</sup> This phase suffers from a small electrical conductivity, caused by the small carrier concentration. By contrast, the hexagonal phase reveals a large electrical conductivity, but a small Seebeck coefficient. Hence both phases only possess a small power factor. On the contrary, the rhombohedral phase features a much larger power factor. In particular, one notes in Figure 2, that the transition from the hexagonal to the rhombohedral phase is accompanied by a huge increase of the power factor by about 900–1000%. Such an observation is ideally suited to unravel the causes of large power factors. Both rhombohedral and hexagonal phases behave like degenerate semiconductors and share hole concentrations of about  $5 \times 10^{21} \text{ cm}^{-3}$ . Hence, the large change in the power factor cannot be attributed to differences in the concentration of charge carriers. Comparison of the Seebeck coefficient and the electrical conductivity of the two phases shows that the latter only decreases by a factor of about 2 upon the transition to the rhombohedral phase, while the Seebeck coefficient increases by a factor of around 4.5; this leads to the strong contrast in the power factor. Hence, we need to understand the origin of the difference in Seebeck coefficient and electrical conductivity between the two phases.

The simplest description of Seebeck coefficient and electrical conductivity of metals and degenerate semiconductors is provided by the Pisarenko<sup>[38]</sup> and the Drude formula<sup>[39]</sup>

$$S = \frac{8\pi^2 k_B^2}{3eh^2} m_{\text{DOS}}^* T \left( \frac{\pi}{3n} \right)^{2/3} \quad (2a)$$

$$\sigma = e\mu n = e \frac{e\tau}{m_{\text{Drude}}^*} n \quad (2b)$$

where  $m_{\text{DOS}}^*$  is the density of states effective mass,<sup>[40]</sup>  $m_{\text{Drude}}^*$  is the conductivity effective mass,<sup>[41]</sup>  $n$  is the carrier concentration,

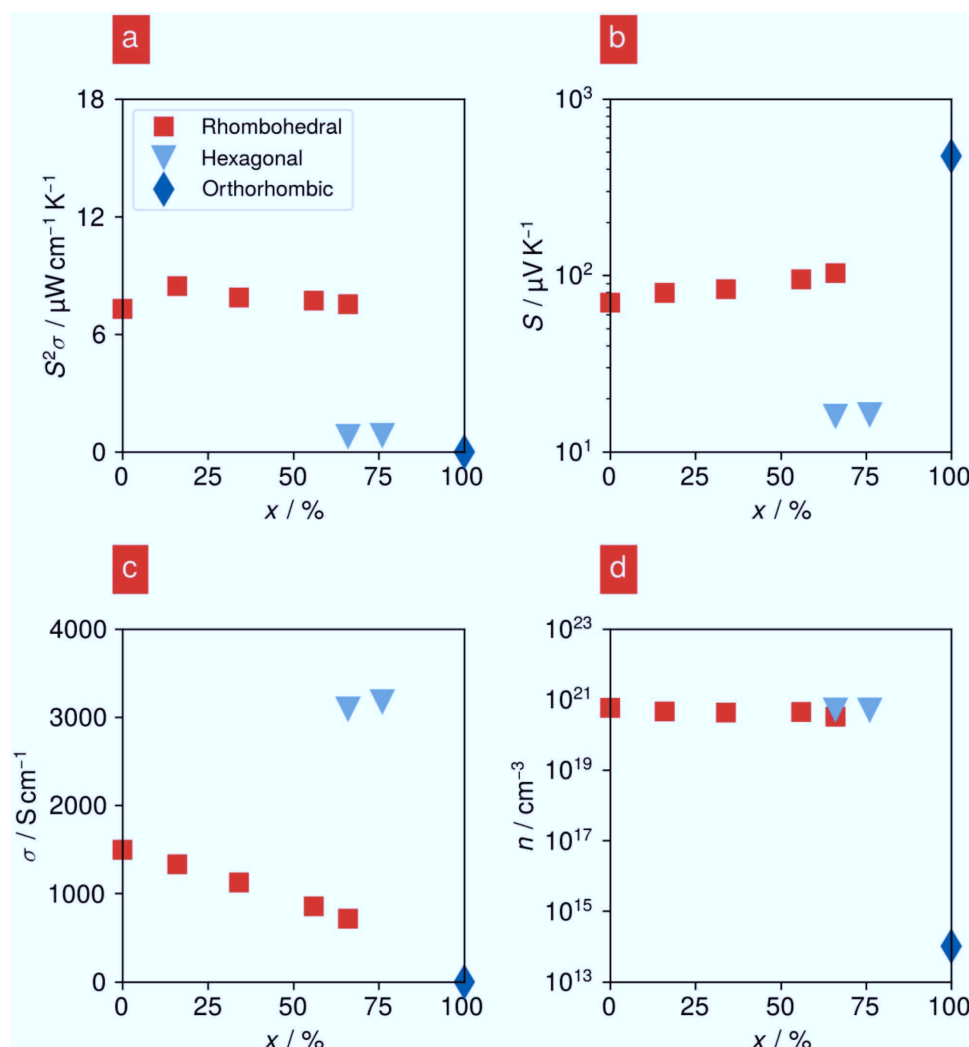


**Figure 2.** Electronic transport properties in crystalline  $\text{GeSe}_x\text{Te}_{1-x}$  alloys. a) Power factor  $S^2\sigma$ , b) Seebeck coefficient  $S$ , c) electrical conductivity  $\sigma$ , and d) carrier concentration at room temperature as a function of stoichiometry and crystal structure. The rhombohedral phase exhibits a power factor which exceeds the hexagonal phase by 900–1000%. Comparing the Seebeck coefficient and the electrical conductivity for both phases shows that the latter only decreases by a factor of about 2 upon the transition to the rhombohedral phase, while the Seebeck coefficient increases by a factor of around 4.5. Nevertheless, the carrier concentration is comparable and hence not responsible for the huge difference in power factor. Instead, the superior thermoelectric performance of the rhombohedral phase must be associated to features of the band structure, which decouple the decrease in conductivity from the increase in Seebeck coefficient.

$\mu$  is the carrier mobility,  $\tau$  is the carrier relaxation time,  $T$  is the temperature,  $k_B$  is Boltzmann's constant,  $e$  is the elementary charge, and  $h$  is Planck's constant. The strong screening associated to the very large polarizabilities found in phase-change materials<sup>[28,42]</sup> makes electron–electron interactions negligible,<sup>[43]</sup> hence justifying Equation (2). Accordingly, the power factor only depends upon the concentration of charge carriers, their relaxation time, the two different effective masses  $m_{\text{DOS}}^*$  and  $m_{\text{Drude}}^*$  as well as temperature. For a single and parabolic band (SPB),  $m_{\text{DOS}}^* = m_{\text{Drude}}^*$ .<sup>[44]</sup> Rhombohedral and hexagonal phases exhibit comparable carrier concentrations, with the latter having a mobility that is 2–3 times larger (see Figure S4, Supporting Information). However, the power factor is much larger in the rhombohedral phase. According to Equation (2), this implies that these two types of effective mass must differ.  $m_{\text{DOS}}^*$  and  $m_{\text{Drude}}^*$  are generally dependent on the features of the band

structure around the Fermi level<sup>[45,46]</sup> and their comparison can reveal important information crucial to understand the thermoelectric performance. Yet, the ratio  $m_{\text{DOS}}^*/m_{\text{Drude}}^*$ , which can be considered as a figure of merit of the band structure for high power factors, has not been employed so far in experimental studies of the thermoelectric performance.

Thus, techniques are needed which can determine both  $m_{\text{DOS}}^*$  and  $m_{\text{Drude}}^*$ .  $m_{\text{DOS}}^*$  can be obtained by fitting Seebeck coefficient and carrier concentration versus temperature according to Equation (2a). Once electrical conductivity and carrier concentration are known,  $m_{\text{Drude}}^*$  can be determined with the addition of optical reflectivity measurements: a) from the plasma frequency  $\omega_p = \sqrt{ne^2/(\epsilon_0 m_{\text{Drude}}^*)}$  of free carriers, b) from the carrier mobility and the damping  $\omega_d = 1/\tau$  of free carriers. The combination of electrical conductivity, Hall and Seebeck measurements with the optical reflectivity thus provides important information

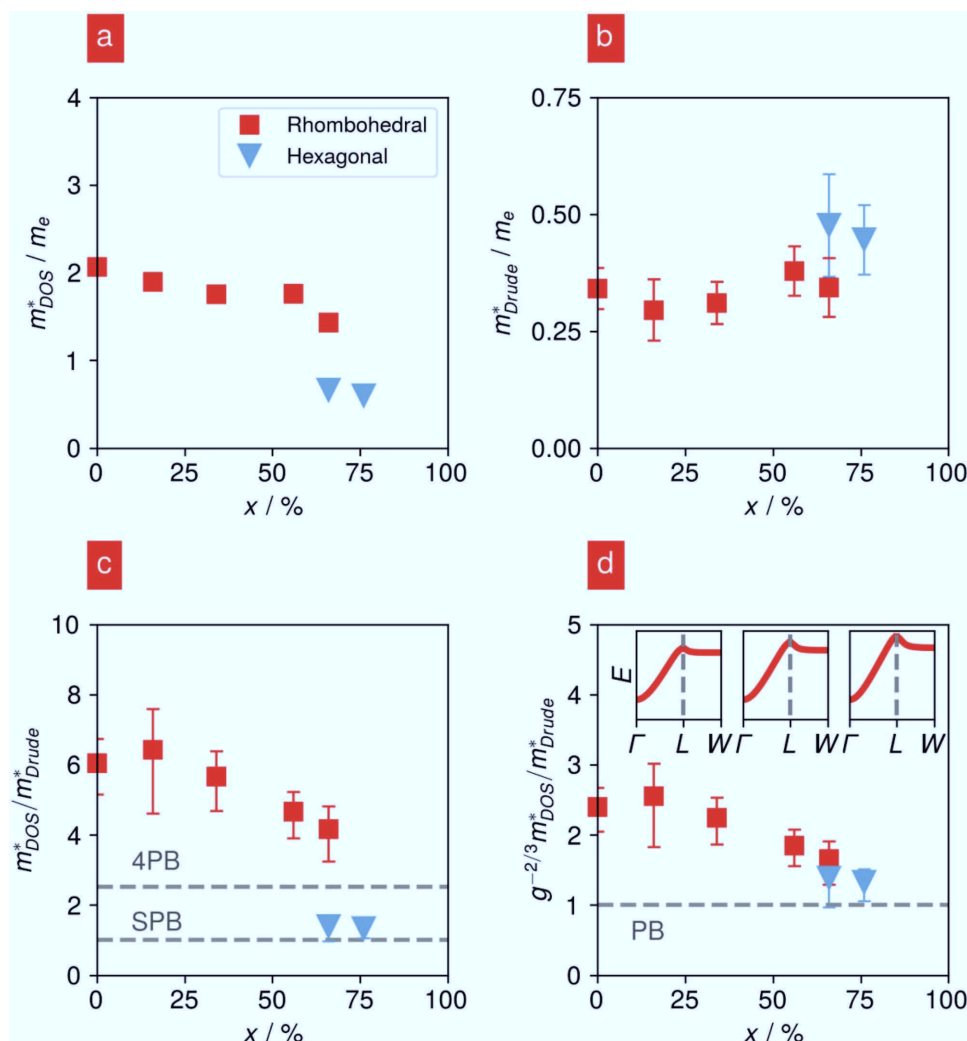


**Figure 3.** Effective masses in crystalline  $\text{GeSe}_x\text{Te}_{1-x}$  alloys. a) Density-of-states effective mass  $m_{\text{DOS}}^*$ , b) conductivity effective mass  $m_{\text{Drude}}^*$ , c) figure of merit  $m_{\text{DOS}}^*/m_{\text{Drude}}^*$  and d)  $m_{\text{DOS}}^*/m_{\text{Drude}}^*$  normalized to the valley degeneracy as a function of stoichiometry and crystal structure. Ideal values for the single-parabolic-band (SPB) and the four-parabolic-bands (4 PB) models are reported as dashed lines for comparison. The behavior of the hexagonal phase can be explained within an SPB picture. On the other hand, the rhombohedral phase exhibits a figure of merit which cannot be explained by an SPB. This is due to: 1) the fourfold degeneracy of the band valleys relevant for transport, as well as 2) the strong anisotropy of such band valleys. The superior power factor  $S^2\sigma$  results from a combination of both effects. The reduced anisotropy within the rhombohedral phase for increasing selenium content is in line with a gradual change of bonding, as suggested by Figure 1, and the resulting changes of band structure, as sketched in the insets of (d).

on the band structure around the Fermi energy. The results are reported in **Figure 3**, together with the ratio  $m_{\text{DOS}}^*/m_{\text{Drude}}^*$ . The data presented in this figure provide several important insights. For the hexagonal phase, the SPB model is sufficient to describe electron transport since  $m_{\text{DOS}}^*/m_{\text{Drude}}^* = 1$ . In the rhombohedral phase, on the other hand,  $m_{\text{DOS}}^*/m_{\text{Drude}}^*$  is much larger than 1. Therefore, the SPB model fails in describing the power factor of the rhombohedral phase. This scenario occurs when charge carriers are located at degenerate and/or anisotropic band valleys. The collective action of  $g$  degenerate ellipsoidal band valleys leads to a breakdown of the SPB model and to more general formulas for the effective masses which enter Equation (2)<sup>[47,48]</sup>

$$m_{\text{DOS}}^* = g^{2/3} (m_1^* m_2^* m_3^*)^{1/3} \quad (3a)$$

$$m_{\text{Drude}}^* = 3 \left( \frac{1}{m_1^*} + \frac{1}{m_2^*} + \frac{1}{m_3^*} \right)^{-1} \quad (3b)$$

where  $m_i^*$  are the effective masses along the principal axes of the ellipsoid. According to Equations (2) and (3), the trade-off between Seebeck coefficient and electrical conductivity imposed by a single parabolic band ( $m_{\text{DOS}}^* = m_{\text{Drude}}^*$ ) can be overcome by a large valley degeneracy  $g$ . To the same end, a strong anisotropy of the band valleys can lead to a large difference between  $m_1^*$ ,  $m_2^*$ , and  $m_3^*$  and make  $(m_1^* m_2^* m_3^*)^{1/3} \propto m_{\text{DOS}}^*$  much larger than  $\left( \frac{1}{m_1^*} + \frac{1}{m_2^*} + \frac{1}{m_3^*} \right)^{-1} \propto m_{\text{Drude}}^*$ . Since  $S^2\sigma \propto m_{\text{DOS}}^*/m_{\text{Drude}}^*$ , the simultaneous realization of a heavy  $m_{\text{DOS}}^*$  and a light  $m_{\text{Drude}}^*$  leads to a superior power factor.

Both degeneracy and anisotropy are at play for rhombohedral IV–VI compounds. Their crystal structure is a small

distortion of the rock-salt crystal structure.<sup>[26]</sup> Accordingly, the band structure of rhombohedral GeTe is a weakly perturbed version of the band structure of cubic GeTe.<sup>[49]</sup> Therefore, it is reasonable to adopt a rock-salt crystal structure in the following discussion for simplicity. For IV–VI compounds with rock-salt like crystal structure, the valence band maximum is at the L-point of the Brillouin zone.<sup>[50]</sup> Hence, the charge carriers are located at the L-point, if we have p-doped materials, which is frequently the case in the chalcogenides studied here. The symmetry operations of the point group transform the L-point into itself and three inequivalent points of the Brillouin zone leading to a value for  $g$  equal to 4 that enhances the power factor by  $\approx 2.5$  times. However,  $m_{\text{DOS}}^*/m_{\text{Drude}}^*$  takes values between 4 and 7. Hence the strong anisotropy of the band valley around the L-point<sup>47</sup> must enlarge  $m_{\text{DOS}}^*/m_{\text{Drude}}^*$  as compared to the value predicted by a four-parabolic-bands model (4 PB), as shown in Figure 3. As a matter of fact, the effective mass tensor has a heavy component along  $\Gamma$ -L, a light one along L-W.<sup>[51]</sup> According to Equation (3), the light component dominates the conductivity effective mass, while the heavy component ensures values larger than  $g^{2/3}m_{\text{Drude}}^*$  (i.e., about 2.5  $m_{\text{Drude}}^*$ ) for the density-of-states effective mass. Hence, the strong anisotropy of the band valley boosts the power factor.

Within a linear combination of atomic orbitals<sup>[52]</sup> framework, such anisotropy depends upon the orbital energies of the constituent atoms and their bond energies, which provide the energy dispersion relation  $E(\mathbf{k})$  around the L-point. We will now relate the observed band structure features to such a chemical-bonding perspective. Understanding properties from a chemical bonding perspective is very promising, since it allows systematic trends with stoichiometry to be predicted, hence aiding the design of complex alloys with tailored properties. Such a description of the electronic properties of (pseudo-) binary chalcogenides, which are relevant for their thermoelectric performance, is still missing. Hence, we try to fill this gap to obtain atomistic design rules for thermoelectric applications. The theoretical tool utilized here is the semiempirical tight-binding method.<sup>[53–55]</sup> This is the simplest model which is able to describe the experimental data reported in the present work.

IV–VI compounds with octahedral coordination exhibit a rock-salt like structure with the IV atom playing the formal role of the cation and the VI atom that of the anion. Nevertheless, in these materials there is no significant charge transfer between the atoms and hence the bonding is not ionic. Each atom possesses an average of three valence p-electrons and is connected to its six nearest neighbors through an average of one electron per bond.<sup>[25]</sup> This configuration is intermediate between covalent and metallic bonding and leads to the establishment of metavalent bonding; the presence of metavalent bonding in the rock-salt like GeSe<sub>x</sub>Te<sub>1-x</sub> alloys under study has been already confirmed by previous studies.<sup>[29,31]</sup> The bonding orbitals are mainly formed from p-orbitals in  $\sigma$ -bonding configuration, with weak s-p hybridization and small charge transfer, as can be seen in Figure 1. To describe the main features of the valence band, one can start from a tight-binding model built from p-orbitals.<sup>[56,57]</sup> The energy dispersion relation of the  $p_x$  valence band can be written as

$$E(\mathbf{k}) = -\sqrt{\epsilon^2 + 4t_\sigma^2 \cos^2 \frac{k_x a}{2}} \quad (4)$$

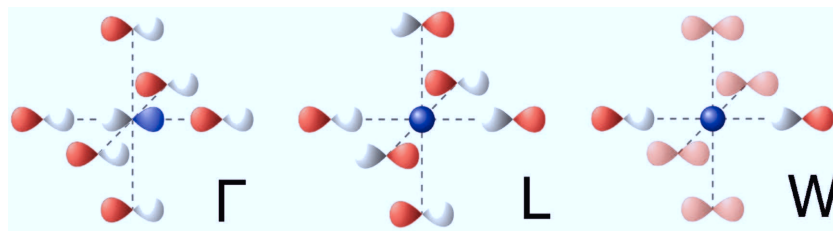
$t_\sigma$  is the bond energy between p-orbitals of nearest neighbors in  $\sigma$ -bonding configuration, while  $\epsilon$  describes the ionicity, corresponding to half of the energy difference between cation and anion p-orbitals;  $a$  is the lattice constant. Permutation of indices provides the  $p_y$  and  $p_z$  valence bands. The resulting threefold degeneracy along the  $\Gamma$ -L direction and the lack of dispersion of the  $p_x$  band along the L-W direction are inconsistent with band structure calculations.<sup>[58]</sup> The issue can be solved by extending the model to include further effects. First, one can take second-nearest neighbor interactions into account. This is reasonable since metavalent materials exhibit long-range interactions.<sup>[23,59]</sup> This is accomplished through the introduction of a nonzero bond energy  $\gamma$  between p-orbitals of adjacent VI atoms.<sup>[60]</sup> Second, one can take into account hybridization between the s-state of IV atoms and the p-states of surrounding VI atoms.<sup>[21,61]</sup> The corresponding bond energy is denoted as  $\eta$ , while  $h$  is half of the energy difference between such states. This extended model exhibits additional nonvanishing matrix elements that make the diagonalization of the Hamiltonian matrix more challenging. Nevertheless, it is possible to derive the eigenvalues at the high-symmetry points  $\Gamma$ , L, and W of the Brillouin zone. The results obtained are summarized in Table 1, where they are compared to the description provided by Equation (4). More details about the model can be found in the Supporting Information.

We can now analyze the equations in Table 1 and their consequences for the effective mass of the charge carriers. The curvature of the energy dispersion relation  $E(\mathbf{k})$  around the L-point provides the effective mass tensor for charge carriers, hence we consider the two high symmetry directions  $\Gamma$ -L and L-W in the following. Curvature changes as function of the bonding parameters can thus be deduced by considering the eigenvalues at the end points  $\Gamma$ , L, and W. Materials in the left lower corner of the map in Figure 1 are characterized by small ionicity and little s-p hybridization. s-p hybridization increases the electron energy at the L-point, creating the valence-band maximum. The curvature of the valence band around L is small along  $\Gamma$ -L, large along L-W,<sup>[51]</sup> hence  $m_{\text{DOS}}^*/m_{\text{Drude}}^*$  is large. Such condition is favorable to achieve large power factors. Both increasing s-p mixing (decreasing  $h$ , increasing  $\eta$ ) and increasing ionicity (increasing  $\epsilon$ ) reduce the anisotropy of the band valley at the L-point, though in different ways. The former does it by increasing the bandwidth along  $\Gamma$ -L and L-W, the increase being stronger along  $\Gamma$ -L than along L-W, as shown by the dependence of  $E$  on  $h$  and  $\eta$ . The latter does it in a less straightforward manner and can be understood by considering the  $a^{-n}$  dependence of the tight-binding parameters  $t_\sigma$ ,  $\eta$ , and  $\gamma$ .<sup>[62]</sup> According to Table 1, increasing  $\epsilon$  alone compresses the band valley along  $\Gamma$ -L and enhances anisotropy. However, it also reduces the lattice constant  $a$  because of the larger electronegativity difference between the constituent atoms.<sup>[63]</sup> The corresponding increase of  $t_\sigma$  significantly reduces the energy at  $\Gamma$  and increases the band width along  $\Gamma$ -L. The overall effect is a reduction of the anisotropy of the effective mass tensor. These mechanisms lead to a smaller  $m_{\text{DOS}}^*/m_{\text{Drude}}^*$ , which is detrimental for the power factor. These observations, in line with values for the tight-binding parameters reported in literature,<sup>[64]</sup> are sketched in Figure 4, which displays the qualitative predictions obtained by our model. Progressive substitution of Te with



**Table 1.** Upper valence band at the high-symmetry points of the Brillouin zone of rock-salt IV–VI compounds. The table provides analytic formulas for the energy of the electrons occupying the upper valence band of IV–VI compounds. The equations presented are obtained by the tight-binding method. The simplest possible model described by Equation (3), which accounts only for interactions between nearest-neighbor p-orbitals ( $t_\sigma > 0$ ), is compared to the more refined model accounting for interactions between second-nearest-neighbor p-orbitals ( $\gamma > 0$ ) and between nearest-neighbor s- and p-orbitals ( $\eta > 0$ ).  $\epsilon$  is half of the energy difference between IV p and VI p atomic states,  $h$  is half of the energy difference between IV s and VI p atomic states. A sketch of how the atomic orbitals interact to provide the electron energy at the high-symmetry points is also presented; the wave function is complex-valued for the atomic orbitals in light red.

$E(\Gamma) =$	$-\sqrt{\epsilon^2 + 4t_\sigma^2}$	for $\gamma = 0, \eta = 0$
	$-\sqrt{(\epsilon - 2\gamma)^2 + 4t_\sigma^2} + 2\gamma$	for $\gamma > 0, \eta > 0$
$E(L) =$	$-\epsilon$	for $\gamma = 0, \eta = 0$
	$-\epsilon - 2\gamma - h + \sqrt{(h - 2\gamma)^2 + 12\eta^2}$	for $\gamma > 0, \eta > 0$
$E(W) =$	$-\epsilon$	for $\gamma = 0, \eta = 0$
	$-\epsilon - h + \sqrt{h^2 + 4\eta^2}$	for $\gamma > 0, \eta > 0$



Se gradually strengthens s-p hybridization and charge transfer. This results in a reduction of the anisotropy of the band valley at the L-point, hence a decreasing  $m_{\text{DOS}}^*/m_{\text{Drude}}^*$ . Therefore, our model can readily explain the behavior of  $m_{\text{DOS}}^*/m_{\text{Drude}}^*$  observed within the rhombohedral phase. Hence, compounds with band structures more suitable to obtain a large  $m_{\text{DOS}}^*/m_{\text{Drude}}^*$  through anisotropy of the effective mass tensor are found in the lower left corner of the map in Figure 1.

We can hence conclude that the symmetry properties of the L-point create a large valley degeneracy of 4, while  $\sigma$ -orbitals from aligned p electrons lead to a stronger anisotropy of such valleys: the power factor is thus strongly enhanced. Perturbation of such configurations due to increased s-p mixing and ionicity is detrimental to the thermoelectric performance, as confirmed by the progressive reduction of  $m_{\text{DOS}}^*/m_{\text{Drude}}^*$  within the rhombohedral phase for increasing Se content. The hexagonal phase has a lower degeneracy, and its structure suggests strong s-p mixing, which should lead to a highly isotropic valley. Again, the model produces conclusions consistent with our experimental data.

In summary, we have identified and explained a link between the chemical bonding and the thermoelectric power factor

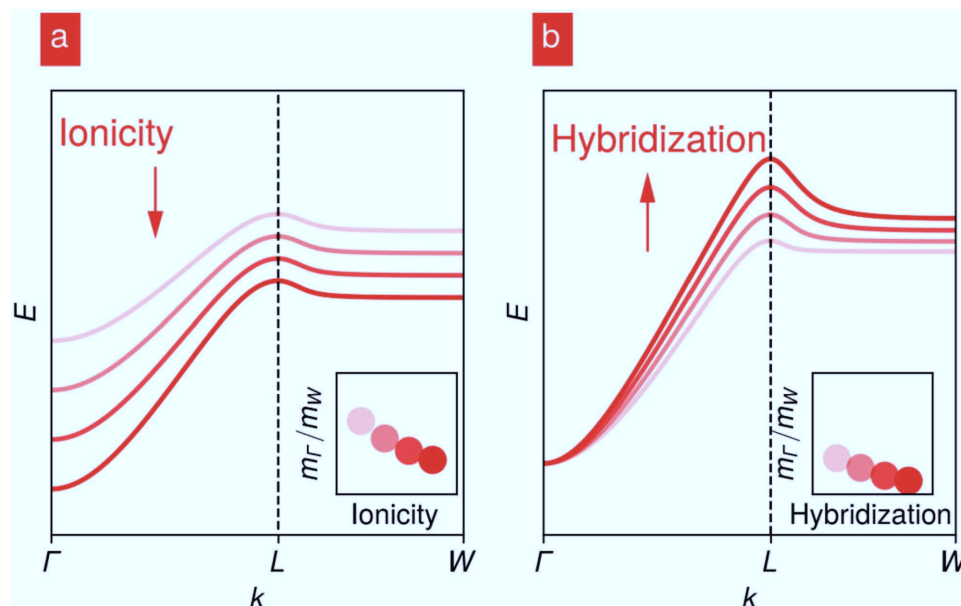


**Figure 4.** Effect of the chemical bonding parameters on the valence band at the L-point. a) Effect of ionicity, and b) effect of s-p mixing; the arrows point toward the direction of increasing values for both quantities. Increasing ionicity compresses the band valley along  $\Gamma$ -L because of a larger  $\epsilon$ . However, the subsequent reduction of  $a$  leads to a larger  $t_\sigma$ . The overall result is a larger bandwidth along  $\Gamma$ -L. Increasing s-p mixing increases the bandwidth along  $\Gamma$ -L and L-W, the increase being stronger along  $\Gamma$ -L than along L-W. Therefore, both effects are responsible for a reduction of the ratio between the effective mass along  $\Gamma$ -L,  $m_\Gamma$ , and the effective mass along L-W,  $m_W$ , obtained from the directional second derivatives of  $E(k)$ ; this is shown in the insets. This results in a smaller  $m_{\text{DOS}}^*/m_{\text{Drude}}^*$ .

of IV–VI compounds. The octahedral-like coordination in chalcogenides with rhombohedral phase, which accompanies systems with metavalent bonding, results in a highly symmetric crystal structure. This leads to a large degeneracy of the band valleys relevant for transport, which enhances the ratio  $m_{\text{DOS}}^*/m_{\text{Drude}}^*$ , and hence the power factor, by 2.5 times with respect to a single parabolic band. In addition, weak s-p hybridization and small charge transfer result in a strong band anisotropy of such valleys that further increase the ratio  $m_{\text{DOS}}^*/m_{\text{Drude}}^*$ , leading to an overall enhancement of the power factor by 4 to 7 times. These two effects provide intrinsic material properties that boost the power factor  $S^2\sigma$ . Hence we obtain simple atomistic design rules for IV–VI compounds and related alloys, which aim at tuning the band structure in order to achieve a good thermoelectric performance. The insights presented here relating chemical bonding and thermoelectric performance of IV–VI compounds are also supported by the map in Figure 1. Chalcogenides with intrinsically good thermoelectric performance are found closer to the origin, where metavalent bonding prevails and charge transfer and s-p mixing are weaker. It is important to note that the present map is not able to distinguish between different structures with the same stoichiometry, since its axes are defined by atomic quantities.<sup>[65]</sup> Hence, the present work should trigger follow-up projects aimed at defining new coordinates that account for different crystal structures. Furthermore, the approach presented here can be applied for other material classes with thermoelectric behavior, such as  $\text{V}_2\text{VI}_3$ <sup>[1,38]</sup> and  $\text{I–V–VI}_2$ <sup>[8,21]</sup> compounds, in order to identify new thermoelectric materials. Linking chemical bonding parameters to microscopic quantities such as valence energy levels will enable the definition of maps for properties related to the thermoelectric performance, which provide predictive power and aid the design of new thermoelectric materials.

Finally, it is important to remark that parabolic-band models, though widely used, cannot account for all the features responsible for the enhancement of the thermoelectric performance. Our experimental data clearly prove the crucial role of the anisotropy of the effective mass tensor in enhancing the thermoelectric performance. At the same time, our elementary model provides simple design rules aimed at optimizing such anisotropy in order to maximize the thermoelectric performance. Hence, we suggest a revival of the combination of electrical transport and reflectivity measurements, together with atomistic modeling of the band structure, as driving force in the search of new material systems with high thermoelectric performance.

## Experimental Section

**Sample Preparation:** 500 nm thin films of  $\text{GeSe}_x\text{Te}_{1-x}$  alloys were deposited from stoichiometric GeTe and GeSe targets by DC magnetron cosputtering deposition (background pressure  $2 \times 10^{-6}$  mbar, Ar flow 20 sccm, deposition rate  $< 1 \text{ \AA s}^{-1}$ ). To obtain nonoriented polycrystalline samples, the as-deposited amorphous films were annealed under Ar atmosphere. For the rhombohedral phase, GeTe,  $\text{GeSe}_{0.16}\text{Te}_{0.84}$ , and  $\text{GeSe}_{0.34}\text{Te}_{0.66}$  have been annealed for 30 min respectively at 225, 250, and 300 °C,  $\text{GeSe}_{0.56}\text{Te}_{0.44}$  and  $\text{GeSe}_{0.66}\text{Te}_{0.34}$  were annealed for 2 min at 325 °C. For the hexagonal phase,  $\text{GeSe}_{0.66}\text{Te}_{0.34}$  and  $\text{GeSe}_{0.76}\text{Te}_{0.24}$  were annealed for 20 h at 325 °C. Stoichiometry and phase of the thin

films were checked by energy dispersive X-ray spectroscopy and X-ray diffraction. For FTIR measurements, the thin films were sputtered on highly resistive double side polished silicon substrates. For Seebeck coefficient measurements, 20 mm stripes of  $\text{GeSe}_x\text{GeTe}_{1-x}$  thin films were deposited onto Corning 1737 glass slides with gold contact stripes.<sup>[33]</sup> For two-point resistance and Hall measurements, the thin films were deposited onto a glass substrate with gold contacts in a Hall bar geometry.<sup>[66]</sup> The thickness of the films were determined on reference samples by Bruker DektakXT stylus profiler.

**Charge Transport Measurements:** The Seebeck coefficient  $S$  was measured in the temperature range of 20–100 °C with a custom-built setup. Electrical conductivity  $\sigma$  and carrier concentration  $n$  in the same temperature range were determined from two-point resistance measurements and Hall measurements performed on the Hall bar samples with a PPMS setup from Quantum Design. Data for GeSe were taken from literature.<sup>[35]</sup> The experimental curves  $S \cdot n^{2/3}$  versus  $T$  were fitted to a straight line and  $m_{\text{DOS}}^*$  were determined from the calculated slope, according to Equation (2a).

**Optical Characterization:** Room-temperature reflectivity spectra were measured in the energy range of 400–8000  $\text{cm}^{-1}$  by Bruker IFS 66v/S and Bruker Vertex 70 FTIR spectrometers, with an incident angle of 10° in the IFS 66v/S, 13° in the Vertex 70; the beam reflected in the specular direction was recorded. For normalization, the measured spectra were divided by the spectrum of a reference gold sample. The spectra were analyzed with the software SCOUT (W. Theiss, Hard- and Software), by using the following model<sup>[28]</sup> for the dielectric function of  $\text{GeSe}_x\text{Te}_{1-x}$

$$\epsilon(\omega) = \epsilon_{\text{const}} + \epsilon_{\text{Tauc-Lorentz}}(\omega; \omega_0, S, \gamma, \omega_g) + \epsilon_{\text{Drude}}(\omega; \omega_p, \omega_d) \quad (5)$$

where  $\epsilon_{\text{const}}$  is a constant that accounts for the polarizability in the higher energy range,  $\epsilon_{\text{Tauc-Lorentz}}$  describes the onset of optical transitions and  $\epsilon_{\text{Drude}}(\omega)$  is the contribution of free carriers.

Upper and lower limits of the conductivity effective mass were determined from the formulas

$$m_{\text{Drude}}^* = \frac{ne^2}{4\pi^2 c_0^2 \epsilon_0 \omega_p^2} \quad (6)$$

$$m_{\text{Drude}}^* = \frac{e^2 n}{2\pi c_0 \sigma \omega_\tau} \quad (7)$$

where  $e$  is the elementary charge,  $c_0$  is the speed of light in vacuum,  $\epsilon_0$  is the vacuum permittivity,  $n$  is the carrier concentration determined by Hall measurements,  $\omega_p$  and  $\omega_d$  are plasma frequency and damping of free carriers determined by optical measurements.

## Supporting Information

Supporting Information is available from the Wiley Online Library or from the author.

## Acknowledgements

M.W. acknowledges support by the DFG (SFB 917). Moreover, the research leading to these results has received funding from the European Union Seventh Framework Programme (FP7/2007-2013) under Grant Agreement No. 340698, as well as the Excellence Initiative (Distinguished Professorship) and RWTH Aachen University SEED FUNDS 2016 program. The critical reading of the manuscript by Christophe Bichara, Oana Cojocaru-Miréidin and Carlo Gatti is greatly appreciated. The authors also acknowledge Matti Wirtsohn for performing EDX measurements on the samples and Stefan Jakobs for providing the thermal conductivity data reported in Figure S3 of the Supporting Information.

## Conflict of Interest

The authors declare no conflict of interest.

## Keywords

band structure, chalcogenides, chemical bonding, thermoelectrics

Received: March 20, 2018

Revised: April 18, 2018

Published online: July 5, 2018

- [1] G. J. Snyder, E. S. Toberer, *Nat. Mater.* **2008**, 7, 105.
- [2] X. Zhang, L. D. Zhao, *J. Materiomics* **2015**, 1, 92.
- [3] A. F. Ioffe, *Semiconductor Thermoelements and Thermoelectric Cooling*, Infosearch, London **1957**.
- [4] E. S. Toberer, A. Zevalkink, G. J. Snyder, *J. Mater. Chem.* **2011**, 21, 15843.
- [5] B. C. Sales, D. Mandrus, B. C. Chakoumakos, V. Keppens, J. R. Thompson, *Phys. Rev. B* **1997**, 56, 15081.
- [6] R. Venkatasubramanian, T. Colpitts, E. Watko, M. Lamvik, N. El-Masry, *J. Cryst. Growth* **1997**, 170, 817.
- [7] K. F. Hsu, S. Loo, F. Guo, W. Chen, J. S. Dyck, C. Uher, T. Hogan, E. K. Polychroniadis, M. G. Kanatzidis, *Science* **2004**, 303, 818.
- [8] T. Schröder, T. Rosenthal, N. Giesbrecht, M. Nentwig, S. Maier, H. Wang, G. J. Snyder, O. Oeckler, *Inorg. Chem.* **2014**, 53, 7722.
- [9] W. S. Liu, L. D. Zhao, B. P. Zhang, H. L. Zhang, J. F. Li, *Appl. Phys. Lett.* **2008**, 93, 042109.
- [10] Y. Tang, Z. M. Gibbs, L. A. Agapito, G. Li, H. S. Kim, M. B. Nardelli, S. Curatolo, G. J. Snyder, *Nat. Mater.* **2015**, 14, 1223.
- [11] Z. H. Dughaish, *Phys. B (Amsterdam, Neth.)* **2002**, 322, 205.
- [12] Y. Pei, A. LaLonde, S. Iwanaga, G. J. Snyder, *Energy Environ. Sci.* **2011**, 4, 2085.
- [13] A. D. LaLonde, Y. Pei, G. J. Snyder, *Energy Environ. Sci.* **2011**, 4, 2090.
- [14] H. Wang, Y. Pei, A. D. LaLonde, G. J. Snyder, *Adv. Mater.* **2011**, 23, 1366.
- [15] D. Wu, L. D. Zhao, S. Hao, Q. Jiang, F. Zheng, J. W. Doak, H. Wu, H. Chi, Y. Gelbstein, C. Uher, C. Wolverton, M. G. Kanatzidis, J. He, *J. Am. Chem. Soc.* **2014**, 136, 11412.
- [16] X. Yan, B. Poudel, Y. Ma, W. S. Liu, G. Joshi, H. Wang, Y. Lan, D. Wang, G. Chen, Z. F. Ren, *Nano Lett.* **2010**, 10, 3373.
- [17] L. D. Zhao, S. H. Lo, Y. Zhang, H. Sun, G. Tan, C. Uher, C. Wolverton, V. P. Dravid, M. G. Kanatzidis, *Nature* **2014**, 508, 373.
- [18] Y. Pei, X. Shi, A. LaLonde, H. Wang, L. Chen, G. J. Snyder, *Nature* **2011**, 473, 66.
- [19] H. Wang, Z. M. Gibbs, Y. Takagiwa, G. J. Snyder, *Energy Environ. Sci.* **2014**, 7, 804.
- [20] O. Delaire, J. Ma, K. Marty, A. F. May, M. A. McGuire, M. H. Du, D. J. Singh, A. Podlesnyak, G. Ehlers, M. D. Lumsden, B. C. Sales, *Nat. Mater.* **2011**, 10, 614.
- [21] M. D. Nielsen, V. Ozolins, J. P. Heremans, *Energy Environ. Sci.* **2013**, 6, 570.
- [22] J. P. Heremans, *Nat. Phys.* **2015**, 11, 990.
- [23] S. Lee, K. Esfarjani, T. Luo, J. Zhou, Z. Tian, G. Chen, *Nat. Commun.* **2014**, 5, 3525.
- [24] C. W. Li, J. Hong, A. F. May, D. Bansal, S. Chi, T. Hong, G. Ehlers, O. Delaire, *Nat. Phys.* **2015**, 11, 1063.
- [25] P. B. Littlewood, *J. Phys. C: Solid State Phys.* **1980**, 13, 4855.
- [26] D. Lencer, M. Salinga, B. Grabowski, T. Hickel, J. Neugebauer, M. Wuttig, *Nat. Mater.* **2008**, 7, 972.
- [27] G. Lucovsky, R. M. White, *Phys. Rev. B* **1973**, 8, 660.
- [28] K. Shportko, S. Kremers, M. Woda, D. Lencer, J. Robertson, M. Wuttig, *Nat. Mater.* **2008**, 7, 653.
- [29] S. Jakobs, A. von Hoegen, M. Drögel, C. Stampfer, R. P. S. M. Lobo, A. Piarristeguy, A. Pradel, M. Xu, M. Wuttig, to be published.
- [30] M. Wuttig, V. L. Deringer, X. Gonze, C. Bichara, J. Y. Raty, ArXiv171203588 Cond-Mat **2017**.
- [31] M. Zhu, O. Cojocaru-Mirédin, A. M. Mio, J. Keutgen, M. Küpers, Y. Yu, J. Y. Cho, R. Dronskowski, M. Wuttig, *Adv. Mater.* **2018**, 30, 1706735.
- [32] J. R. Sootsman, D. Y. Chung, M. G. Kanatzidis, *Angew. Chem., Int. Ed.* **2009**, 48, 8616.
- [33] E. R. Sittner, K. S. Siegert, P. Jost, C. Schlockermann, F. R. L. Lange, M. Wuttig, *Phys. Status Solidi A* **2013**, 210, 147.
- [34] E. M. Levin, M. F. Besser, R. Hanus, *J. Appl. Phys.* **2013**, 114, 083713.
- [35] X. Zhang, J. Shen, S. Lin, J. Li, Z. Chen, W. Li, Y. Pei, *J. Materiomics* **2016**, 2, 331.
- [36] H. Wiedemeier, P. A. Siemers, *Modern High Temperature Science*, Humana Press, Clifton, New Jersey **1984**, pp. 395–408.
- [37] M. Küpers, P. M. Konze, S. Maintz, S. Steinberg, A. M. Mio, O. Cojocaru-Mirédin, M. Zhu, M. Müller, M. Luysberg, J. Mayer, M. Wuttig, R. Dronskowski, *Angew. Chem. Int., Ed.* **2017**, 56, 10204.
- [38] C. Wood, *Rep. Prog. Phys.* **1988**, 51, 459.
- [39] N. W. Ashcroft, N. D. Mermin, *Solid State Physics*, Brooks Cole, CA **1976**.
- [40] J. Yan, P. Gorai, B. Ortiz, S. Miller, S. A. Barnett, T. Mason, V. Stevanovi, E. S. Toberer, *Energy Environ. Sci.* **2015**, 8, 983.
- [41] H. A. Lyden, *Phys. Rev.* **1964**, 134, A1106.
- [42] C. Chen, P. Jost, H. Volker, M. Kaminski, M. Wirtsohn, U. Engelmann, K. Krüger, F. Schlich, C. Schlockermann, R. P. S. M. Lobo, M. Wuttig, *Phys. Rev. B* **2017**, 95, 094111.
- [43] T. Siegrist, P. Jost, H. Volker, M. Woda, P. Merkelbach, C. Schlockermann, M. Wuttig, *Nat. Mater.* **2011**, 10, 202.
- [44] W. G. Zeier, A. Zevalkink, Z. M. Gibbs, G. Hautier, M. G. Kanatzidis, G. J. Snyder, *Angew. Chem., Int. Ed.* **2016**, 55, 6826.
- [45] H. D. Barber, *Solid-State Electron.* **1967**, 10, 1039.
- [46] M. A. Green, *J. Appl. Phys.* **1990**, 67, 2944.
- [47] T. Numai, *Laser Diodes and Their Applications to Communications and Information Processing*, John Wiley & Sons, Inc., Hoboken, NJ, USA **2010**, pp. 381–382.
- [48] T. Numai, *Laser Diodes and Their Applications to Communications and Information Processing*, John Wiley & Sons, Inc., Hoboken, NJ, USA **2010**, pp. 383–384.
- [49] H. M. Polatoglou, G. Theodorou, N. A. Economou, *Physics of Narrow Gap Semiconductors*, Springer, Berlin/Heidelberg, Germany **1982**, pp. 221–225.
- [50] Y. W. Tung, M. L. Cohen, *Phys. Rev.* **1969**, 180, 823.
- [51] X. Chen, D. Parker, D. J. Singh, *Sci. Rep.* **2013**, 3, 3168.
- [52] R. Hoffmann, *Angew. Chem., Int. Ed. Engl.* **1987**, 26, 846.
- [53] F. Bloch, *Z. Phys.* **1929**, 52, 555.
- [54] J. C. Slater, G. F. Koster, *Phys. Rev.* **1954**, 94, 1498.
- [55] G. Grosso, G. Pastori Parravicini, *Solid State Physics*, Academic Press, San Diego, CA **2013**.
- [56] B. A. Volkov, O. A. Pankratov, *J. Exp. Theor. Phys.* **1978**, 48, 687.
- [57] B. A. Volkov, O. A. Pankratov, *J. Exp. Theor. Phys.* **1983**, 85, 809.
- [58] Y. Zhang, X. Ke, C. Chen, J. Yang, P. R. C. Kent, *Phys. Rev. B* **2009**, 80, 024304.
- [59] V. L. Deringer, R. P. Stoffel, M. Wuttig, R. Dronskowski, *Chem. Sci.* **2015**, 6, 5255.
- [60] P. B. Littlewood, B. Mihaila, R. K. Schulze, D. J. Sararik, J. E. Gubernatis, A. Bostwick, E. Rotenberg, C. P. Opeil, T. Durakiewicz, J. L. Smith, J. C. Lashley, *Phys. Rev. Lett.* **2010**, 105, 086404.
- [61] Z. Y. Ye, H. X. Deng, H. Z. Wu, S. S. Li, S. H. Wei, J. W. Luo, *Npj Comput. Mater.* **2015**, 1, 15001.
- [62] P. Y. Yu, M. Cardona, *Fundamentals of Semiconductors*, Springer, Berlin **2010**.
- [63] G. Xu, G. Fengsheng, T. Yamaguchi, H. Kan, M. Kumagawa, *Cryst. Res. Technol.* **2006**, 27, 1087.
- [64] J. Robertson, *Phys. Rev. B* **1983**, 28, 4671.
- [65] M. Esser, V. L. Deringer, M. Wuttig, R. Dronskowski, *Solid State Commun.* **2015**, 203, 31.
- [66] H. Volker, P. Jost, M. Wuttig, *Adv. Funct. Mater.* **2015**, 25, 6390.